The Astrophysical Journal, 892:79 (9pp), 2020 April 1 https://doi.org/10.3847/1538-4357/ab77b3

Sympathetic Eruptions of Two Filaments with an Identifiable Causal Link Observed by the Solar Dynamics Observatory

Zhiping Song[1,2], Yijun Hou[2,3], Jun Zhang[1,2], and Peng Wang[1]
[1] School of Physics and Materials Science, Anhui University, Hefei 230601, People's Republic of China; zpsong@ahu.edu.cn
[2] CAS Key Laboratory of Solar Activity, National Astronomical Observatories, Chinese Academy of Sciences, Beijing 100101, People's Republic of China
yijunhou@nao.cas.cn
[3] University of Chinese Academy of Sciences, Beijing 100049, People's Republic of China
Received 2019 October 1; revised 2020 February 11; accepted 2020 February 16; published 2020 March 31

Abstract

Filament eruptions occurring at different places within a relatively short time internal, but with a certain physical causal connection, are usually categorized as sympathetic eruptions. Studies of sympathetic eruptions are not uncommon. However, in these studies the causal links between sympathetic eruptions remain rather speculative. In this work, we present detailed observations of a sympathetic filament eruption event in which an identifiable causal link between two eruptive filaments is observed. On 2015 November 15, two filaments (F1 in the north and F2 in the south) were located at the southwestern quadrant of the solar disk. Their main axes were almost parallel to each other. Around 22:20 UT, F1 began to erupt, forming two flare ribbons. The southwestern ribbon apparently moved southwest and invaded the southeast part of F2. This continuous intrusion caused F2's eventual eruption. Accompanying the eruption of F2, flare ribbons and post-flare loops appeared in the northwest region of F2. Meanwhile, neither flare ribbons nor post-flare loops could be observed in the southeastern area of F2. In addition, the nonlinear force-free field extrapolations show that the magnetic fields above F2 in the southeast region are much weaker than those in the northwest region. These results imply that the overlying magnetic fields of F2 were not uniform. So we propose that the southwest ribbon formed from eruptive F1 invaded F2 from its southeast region with relatively weaker overlying magnetic fields relative to its northwest region, disturbing F2 and leading F2 to eventually erupt.

Unified Astronomy Thesaurus concepts: Solar physics (1476); Solar activity (1475); Solar atmosphere (1477); Solar filaments (1495); Solar filament eruptions (1981)

Supporting material: animations

1. Introduction

Solar filaments are cool and dense plasma suspended in the corona, which are also known as prominences when observed at the limb of the Sun. It is widely accepted that filaments are always located above magnetic polarity inversion lines (PILs). According to their locations, filaments can be divided into three classes: active region filaments forming inside active regions, intermediate filaments arising between active regions, and quiescent filaments located at solar quiescent regions (Zirker et al. 1997; Martin 1998; Mackay et al. 2010). Filament eruptions, solar flares, and coronal mass ejections are often seen as different manifestations of the same physical processes, and filament eruptions are believed to play a key role in the onset of these eruptions (Schmieder et al. 2013; Filippov 2018; Sinha et al. 2019). In the popular filament eruption model a lifting filament stretches its overlying magnetic field lines, creating a current sheet between the anti-parallel field lines, where magnetic reconnection occurs, and then the bulk of the plasma and magnetic structure are ejected into interplanetary space. During a filament eruption, the footprints of the reconnecting overlying magnetic field lines continuously brighten different regions in the chromosphere and are observed as two flare ribbons that spread to both sides of the filament with an apparent motion, while the post-flare loops are the newly formed low-lying loop lines (Kopp & Pneuman 1976; Miklenic et al. 2007; Shibata & Magara 2011; Hou et al. 2016; Yang & Zhang 2018).

The eruptions of stable filaments are triggered by the loss of the balance of forces acting on them (Porfir'eva & Yakunina 2013; Kliem et al. 2014; Zaitsev & Stepanov 2018). Several different mechanisms have been proposed and studied for the initiation of filament eruption, such as flux emergence and cancellation (Zhang et al. 2001; Zheng et al. 2017; Dacie et al. 2018), tether cutting reconnection (Moore et al. 2001; Cheng & Ding 2016; Woods et al. 2018), breakout reconnection (Sterling et al. 2011; Kliem et al. 2013; Sun et al. 2015; Chen et al. 2016), and torus or kink magnetohydrodynamic (MHD) instability (Aulanier et al. 2010; Riley et al. 2011; Hassanin & Kliem 2016; Dechev et al. 2018; Hou et al. 2018; Duchlev et al. 2019). A stable filament can also erupt due to a direct interaction from a surrounding filament, during which the magnetic system of the original stable filament is disturbed by magnetic reconnections. Results from Yang et al. (2017) showed that two nearby filaments, which were almost perpendicular to each other, could gradually approach each other and eventually erupt due to a direct collision between them. Furthermore, a filament could also erupt from the mass injection from a surrounding erupting filament (Su et al. 2007).

In addition to the filament eruptions mentioned above, sympathetic eruptions between filaments are also ubiquitous. These eruptions are defined as consecutive filament eruptions occurring within a short time in different locations but having a certain physical connection (Török et al. 2011; Yang et al. 2012; Jiang et al. 2014; Joshi et al. 2016; Wang et al. 2016;

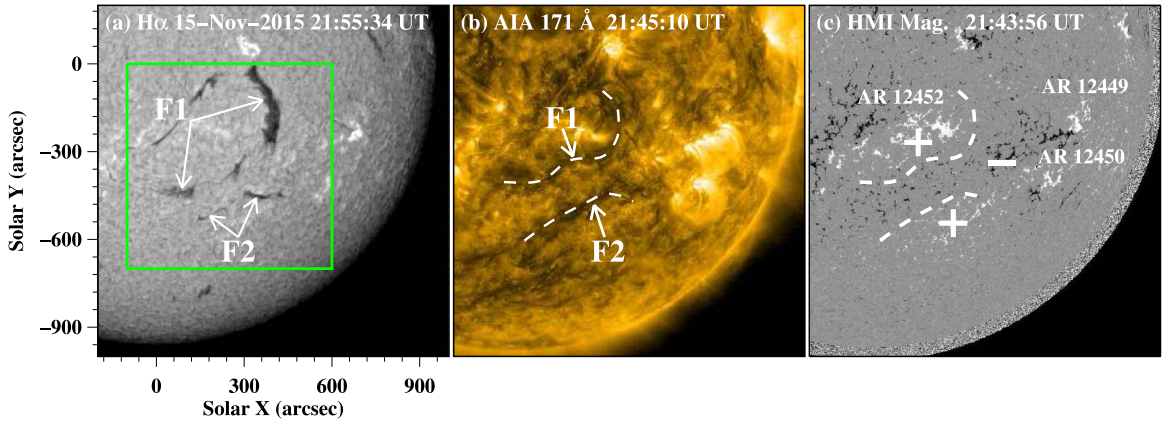

Figure 1. Overview of the two filaments on 2015 November 15. Panel (a): Hα image. The green square in panel (a) outlines the fields of view of panels (a)–(b) in Figure 2, and panels (a1)–(a3) and (b1)–(b3) in Figures 4 and 5. Panel (b): AIA 171 Å image. Panel (c): HMI LOS magnetogram. The two white dashed curves in panels (b) and (c) show the approximate locations of the two nearby filaments before eruptions.

Li et al. 2017). Two filaments, which reside above different PILs and share the same overlying magnetic system, could interact sympathetically, i.e., the first erupting filament disturbs the magnetic system of the second filament and leads to its eruption (Shen et al. 2012). A series of erupting filaments could be connected by magnetic separatrices or quasi-separatrix layers. These filaments could be disturbed by each other and erupt sympathetically via a chain of magnetic reconnections (Schrijver & Title 2011). However, due to the lack of direct observational evidence, it has been debated whether the close temporal correlation between sympathetic eruptions is purely coincidental, or causally linked. The exact mechanism of sympathetic eruptions is still not well understood (Biesecker & Thompson 2000; Török et al. 2011; Wang et al. 2018).

In the present work, we show a detailed process for sympathetic eruptions of two filaments using high-quality data from the Solar Dynamics Observatory (SDO; Pesnell et al. 2012). In this event, a flare ribbon caused by an eruptive filament invaded the location of an adjacent filament and finally led it to erupt. The remainder of this paper is organized as follows. Section 2 describes the observations and data analysis of in our study. In Section 3, we investigate the sympathetic event and present the observation results in detail, followed by a summary and discussion in Section 4.

2. Observations and Data Analysis

We study sympathetic eruptions of two filaments in the southwest quadrant of the solar disk on 2015 November 15–16. The north filament (F1) lies southwest of AR 12452 and the south filament (F2) is located southeast of AR 12449 and AR 12450. They are mainly observed by the SDO/Atmospheric Imaging Assembly (AIA; Lemen et al. 2012) and the SDO/Helioseismic and Magnetic Imager (HMI; Schou et al. 2012). The AIA provides full-disk images taken in 10 extreme ultraviolet (EUV) and ultraviolet (UV) wavelengths. The pixel size and cadence of the EUV images are 0.″6 and 12 s, (24 s for UV wavelengths), respectively. In this study, images in five AIA EUV channels (131 Å, 171 Å, 193 Å, 211 Å, and 304 Å) on 2015 November 15–16 are used for the multi-wavelength analysis of sympathetic eruptions of two filaments. We employ the HMI line-of-sight (LOS) magnetic field data from the SDO to analyze the evolution of the photospheric magnetic fields related to the two filaments. These data have a pixel size of 0.″5 and a cadence of 45 s. The HMI and AIA images are preprocessed by standard routines in the solar software package (SSW), and all the data are differentially rotated to a reference time (00:00 UT on November 16). To investigate the chromosphere configuration of the associated filaments, we also employ corresponding Hα observations from the Global Oscillation Network Group (GONG; Harvey et al. 2011). GONG has collected Hα images observed at seven sites around the world since 2010 and provides successive global Hα observations online.

In order to reconstruct the three-dimensional (3D) magnetic fields above F1 and F2, we perform nonlinear force-free field (NLFFF) extrapolation using the optimization method (Wheatland et al. 2000; Wiegelmann 2004). The boundary condition for the NLFFF extrapolation is an HMI full-disk vector magnetogram with a pixel spacing of 0.″5 at 22:00 UT on 2015 November 15, which is produced using the Very Fast Inversion of the Stokes Vector (VFISV) inversion code every 12 minutes (Borrero et al. 2011). The azimuthal component of the vector field is processed by the minimum energy method to resolve the 180° ambiguity (Metcalf 1994; Leka et al. 2009). Then we transform the vector magnetic field and the geometric mapping of the observed field in the image plane into the heliographic plane (Gary & Hagyard 1990). The NLFFF calculation is conducted within a box of 600 × 552 × 512 uniformly spaced grid points with $dx = dy = dz = 1.''0$. Moreover, we calculate the decay index n of the horizontal magnetic fields above F2, which is defined as $n(z) = -zd\ln(Bh)/dz$ (Kliem & Török 2006) and provides important information about the strapping fields stabilizing the filament.

3. Results

The event analyzed here occurred on 2015 November 15–16. As shown in Figure 1, two sinistral filaments (F1 in the north and F2 in the south) were located in the southwest quadrant of the solar disk. The filament F1 is in the southwest of AR 12452 and the filament F2 was near the southeast of AR 12449 and AR 12450 on November 15. In Hα observations, their lengths are about 500 Mm and 250 Mm, respectively. Two filaments lie above the PILs and their main axes were almost parallel to each other. Filaments F1 and F2 were separated by negative magnetic fields between them.

Since about 22:20 UT on November 15, the northern filament (F1) began to rise quickly and then erupted. After

examining magnetograms and 193 Å images, we noticed that magnetic flux cancellation occurred around barbs of F1 accompanied by 193 Å brightening before F1 eruption (see Figure 2 and online animation of this figure). The fields of view of panels (c1)–(c3) and panels (d1)–(d3) in Figure 2 are outlined by the blue rectangles in panels (a) and (b), respectively. And four sites of flux cancellation along the PIL of F1 are marked by the green boxes, indicating where the magnetic fields with opposite polarities kept approaching each other (see panel (b)). In these four box regions, the magnetograms are replaced by the corresponding HMI magnetograms on November 15 around 20:26 UT, 21:20 UT, 21:56 UT, and 20:35 UT, respectively. To investigate the temporal evolution of the flux cancellation and brightening in detail, we focus on the box region "2." Combining the AIA 193 Å images and HMI magnetograms, one can see that the flux cancellation is accompanied by the EUV brightening. From 17:00 UT to 22:15 UT, the emission enhancement (see panels (c1)–(c3)) as well as the flux cancellation (see panels (d1)–(d3)) continuously appeared in this box region. Along the red line "A–B" shown in panel (d2), we create a time-slice plot (see panel (e)) in HMI LOS magnetograms. Moreover, the 193 Å light curve of the area contoured by the green curve in panel (c3) is superimposed on the time-slice plot (see the green curve in panel (e)). Two magnetic fields with opposite polarities kept approaching each other in box region "2" from 20:00 UT to 24:00 UT. Meanwhile, the emission strength mentioned above continued to enhance from 21:00 UT to 22:20 UT and reached a peak at about 22:20 UT (see the red dotted line in panel (e)).

The F1 eruption is displayed in detail in Figure 3. We focus on the northwest area of F1 (see the field of view marked by the green square in panel (a1)), where the eruption of F1 is most significant, to show the F1 eruption in detail. Since about 22:20 UT, F1 started to rise and then erupted northwest at about 23:00 UT, accompanied by formations of two flare ribbons (outlined by the green dotted curves in panel (a3)). These two flare ribbons appeared on both sides of the magnetic neutral line of F1 and then apparently separated from each other in directions perpendicular to the magnetic neutral line of F1. The northeastern ribbon spread northeast and the southwestern one spread southwest. To study the kinematic evolution of F1, we created time slices from 304, 171, and 131 Å images along the cut "C–D" shown in panel (a2). As displayed by the time-slice plots in panels (b1)–(b3), the filament F1 underwent three kinematic phases: slow rising, accelerating, and constant velocity. By linear fitting, the erupting speeds of F1 during constant velocity phase are estimated as about 100 km s^{-1}. The light curve of 193 Å in the area contoured by the green curve in Figure 2(c3) is superimposed on the time-slice image of 304 Å (see the green curve in panel (b1)). It can be seen that the peak time of brightening and eruptive time of F1 were almost coincident (see the vertical white dotted line in panel (b1)). The F1 eruption is also detailed in the online animated version of Figure 3.

Upon formation, the southwestern flare ribbon related to eruptive F1 (FRF1) continuously moved southwest. At about 23:50 UT, the northwestern part of FRF1 ceased its motion, but the southeastern part of FRF1 kept moving southwest, approaching the site of F2 and invading the location of F2 around 00:18 UT on November 16 (see Figure 4(a1)–(b1)). This intrusion lasted about 100 minutes. After that, filament F2 began to lift slowly, and accelerated to erupt eventually (see panels (b2)–(b3)). In order to investigate the kinematic evolution of F2 in detail, we made time slices (see panels (c1)–(c3)) from 304, 171 and, 131 Å images along a slit "E-F" (see panel (b2)). In panels (c1)–(c3), the dashed curves approximate the tracks of F2 in different wavelengths, and the two vertical green dashed lines indicate the times when F2 began to rise (t1) and to erupt (t2), respectively. We note that F2 appeared as dark belts and it was almost stable before 00:20 UT, when FRF1 reached the site of F2 (panel (b1); see also the green vertical dashed line "t1" in panels (c1)–(c3)). From 00:20 UT to 01:50 UT, F2 rose slowly, accompanied by the successive intrusion of FRF1; the rising speed was about 3 km s^{-1}. At about 01:50 UT, F2 began to rise quickly and then erupted (see the green vertical dashed line "t2" in panels (c1)–(c3)), with speeds of around 120 km s^{-1}. The temporal evolution of FRF1 spreading, the interaction between FRF1 and F2, and the eruption of F2 are shown in the animated version of Figure 4.

Since about 02:10 UT, the eruptive F2 produced two flare ribbons in its northwest area (see the white solid squares in Figure 5), which appeared on both sides of the magnetic neutral line of F2 and then apparently separated from each other in directions perpendicular to the magnetic neutral line of F2 (see panels (a1)–(a3)). The northern ribbon (FRF2) related to F2's eruption approached FRF1, which was formed from F1's eruption. Finally, there is a clear line separating the two approaching ribbons (panel (a3)), implying that there is a magnetic separatrix between the two filaments and F1 and F2 belong to two different magnetic systems. Seen from 171, 131, and 211 Å images, two sets of post-flare loops appeared in the northwest area in gradual phases after the eruptions of F1 and F2. The footpoints of post-flare loops could be identified as the flare ribbons related to the eruptions of F1 and F2. There are two pieces of evidence supporting a correlation between the flare ribbons (post-flare loops) and their corresponding eruptive filaments. The first one is temporal correlation, i.e., FRF1 appeared shortly after the F1 eruption (see Figure 3), and FRF2 immediately followed the eruptive F2 (see Figure 4). The other one is spatial correlation, i.e., the flare ribbons (post-flare loops) formed by different eruptive filaments appeared on both sides of different magnetic neutral lines (see Figure 5). These post-flare loops and their footpoints are displayed in panels (b1)–(b3). It is shown that these loops were rooted in the positive and negative magnetic fields on each side of the two neutral lines. However, we also notice that neither clear flare ribbons nor obvious post-flare loops appeared in the southeast region of F2 (see the dashed–dotted squares in Figure 5). The distribution of flare ribbons and post-flare loops related to eruptive F2 implies that the overlying magnetic fields of F2 are not uniform, and they are weaker in the southeast area but stronger in the northwest region. The temporal evolution of FRF2 and post-flare loops after F2's eruption are also shown in the online animated version of Figure 5.

In order to confirm the non-uniformity of the magnetic fields above F2, We performed NLFFF reconstruction of the overlying magnetic fields of F2 based on the photospheric vector magnetic fields at 22:00 UT on 2015 November 15. Moreover, we calculated the decay index distribution of the reconstructed horizontal magnetic fields above F2. As shown in Figure 6(a), the red-blue curve denotes the magnetic neutral line related to F2, and the blue and red segments correspond to the southeast and northwest regions of F2, respectively. It is obvious that the magnetic fields above F2 in the southeast

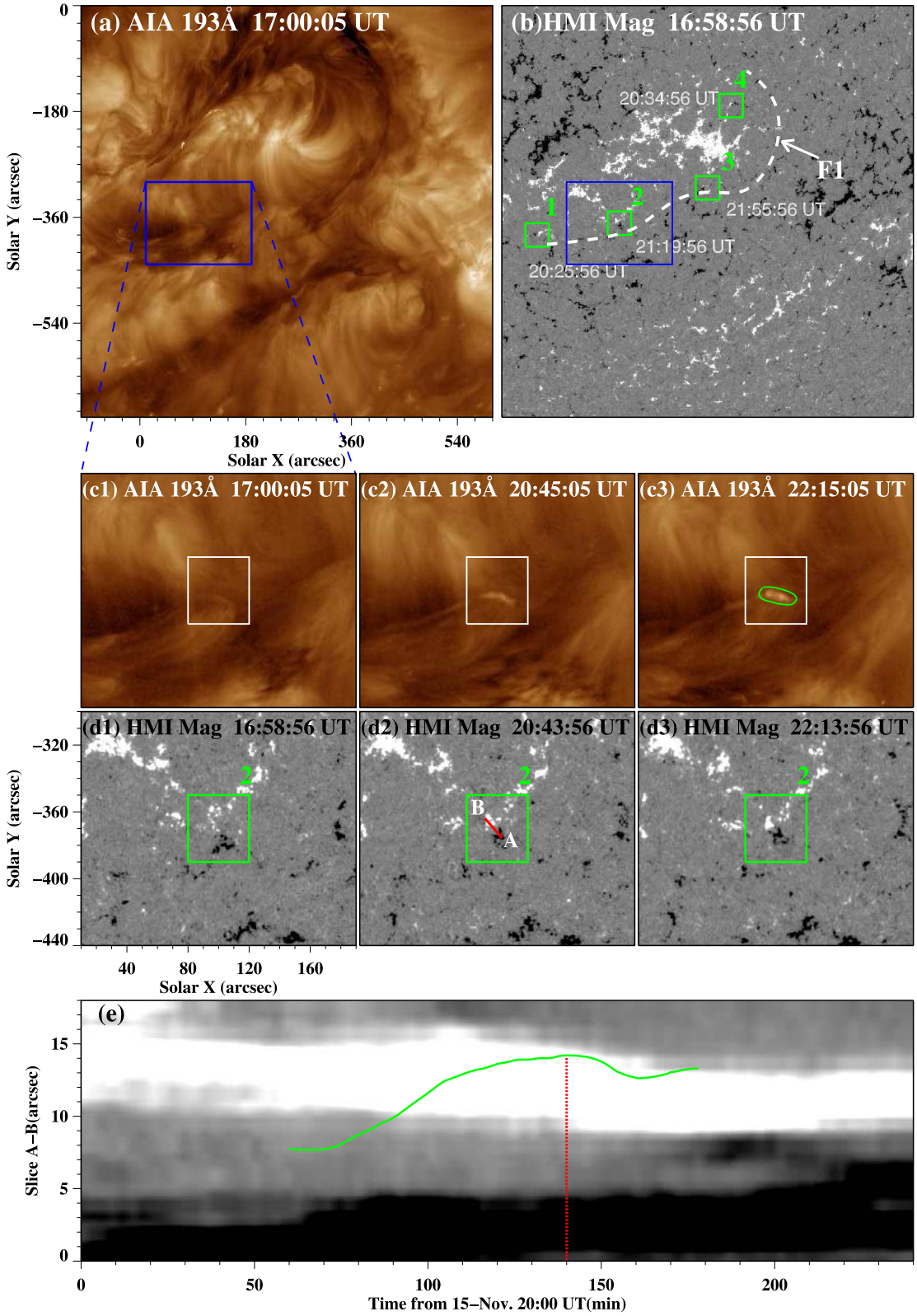

Figure 2. AIA 193 Å images and HMI LOS magnetograms showing the emission brightening and flux cancellation near the barbs of F1. Panels (a) and (b): 193 Å image and HMI magnetogram showing the sites of brightening and flux cancellation. Panels (c1)–(d3): time sequences of 193 Å images and HMI magnetograms showing the temporal evolution of the brightening and flux cancellation, respectively. The white and green squares correspond to the green box "2" in panel (b). The green curve in panel (c3) is the contour of emission strength in 193 Å wavelength. An animation of the AIA 193 Å image and HMI LOS magnetogram is available. It shows the brightening and flux cancellation evolving from 17:00 to 22:50 UT on 2015 November 15. The real time duration of the video is 4 s. Panel (e): time-slice plot of magnetograms along the cut "A-B" marked in panel (d2).

(An animation of this figure is available.)

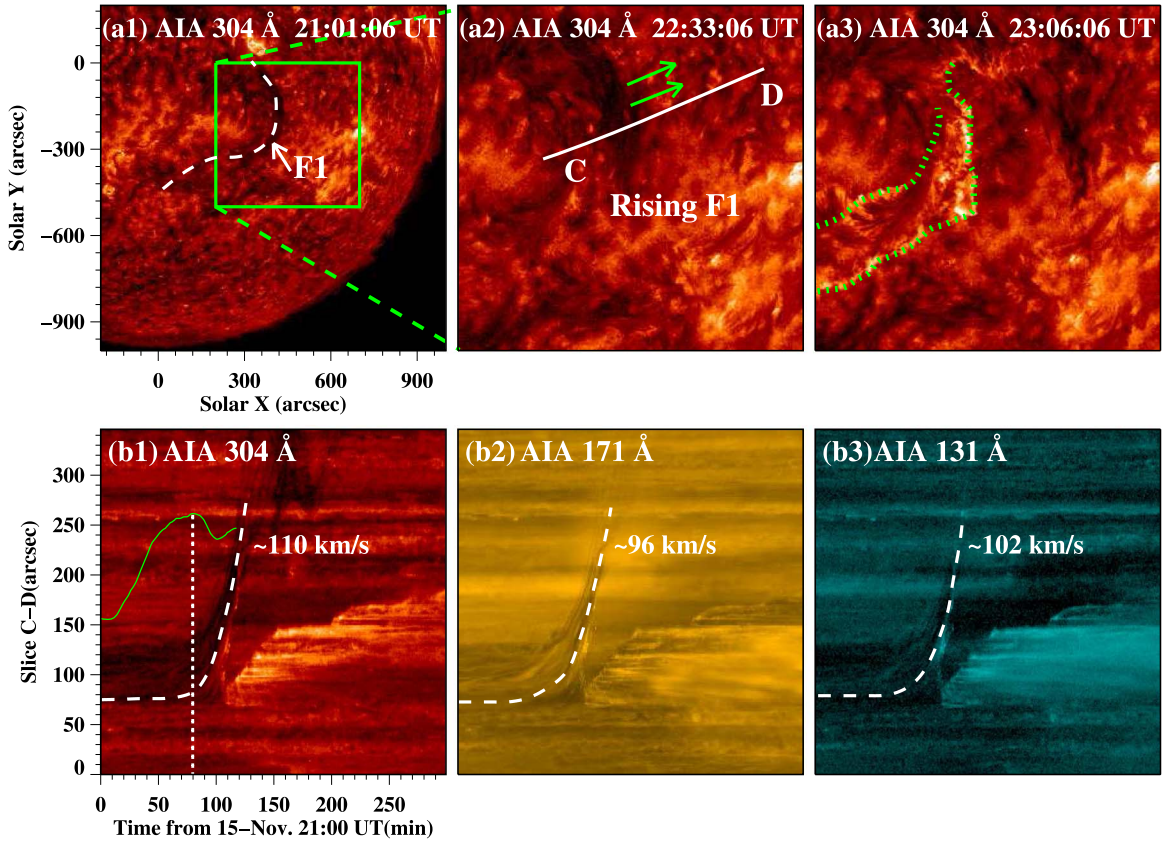

Figure 3. Images of AIA 304 Å and time-slice plots showing the eruption of F1. Panels (a1)–(a3): time sequences of 304 Å images. The green arrows in panel (a2) denote the projected moving directions of F1. The green dotted curves in panel (a3) exhibit two flare ribbons caused by F1 eruption. The line "C-D" in panel (a2) marks the position of time-slice plots in panels (b1)–(b3). Panels (b1)–(b3): time-slice plots of 304, 171, and 131 Å images displaying the temporal evolution of F1. The dashed curves approximate the tracks of F1 in different wavelength images. The green curve in panel (b1) is the 193 Å light curve in the region marked by the green curve in Figure 2(c3). The vertical white dotted line in panel (b1) indicates the time of emission reaching at the peak (the onset of F1 eruption). The animation shows the eruption process of F1 from 22:10 to 23:28 UT on 2105 November 15 in the 304, 171, and 131 Å images. The real time duration of the video is 8 s.

(An animation of this figure is available.)

region are weaker than those in the northwest region (see the green curves). The results shown in panels (b) and (c) also reveal that the decay index of horizontal magnetic fields above F2 in the southeast region is significantly larger than that in the northwest region. This means that the overlying horizontal magnetic fields of F2 decay faster with increasing altitude in the southeast region than in the northwest region. The NLFFF modeling results shown here support the observations and our speculation that the overlying magnetic fields of F2 are not uniform.

4. Summary and Discussion

Using the high-quality data from the SDO, we present eruptive processes of two filaments (F1 and F2) that occurred on 2015 November 15–16. F1 and F2 were separated by negative magnetic fields and their main axes were almost parallel to each other. On November 15, a sequence of emergence and cancellation of the magnetic flux appeared inside the F1 channel and then F1 erupted. The erupting F1 produced two flare ribbons. The southwestern ribbon spread southwest and invaded the southeastern region of F2 for a duration of about 100 minutes, then F2 erupted. The eruptive F2 also produced two flare ribbons in its northwestern region, which moved northward and southward, respectively. During the evolution of these ribbons, a clear separating line manifested between the two nearby ribbons related to the eruptions of F1 and F2, implying that there is a magnetic separatrix between the two filaments and that F1 and F2 belong to different magnetic systems. In gradual phases after the eruptions of F2, post-flare loops appeared in the northwest region of F2, but neither flare ribbons nor post-flare loops were observed in the southeast area of F2. Furthermore, the NLFFF extrapolated 3D magnetic fields and the decay index distribution of the horizontal fields above F2 reveal that the overlying magnetic fields of F2 in the southeast region are weaker than those in the northwest region, and the overlying horizontal magnetic fields of F2 decay faster with increasing altitude in the southeast region than in the northwest region.

The eruptions of filaments are closely connected to the evolution of the magnetic fields underneath, such as magnetic flux emergence and cancellation. The relationship between them has been analyzed in previous studies (Mandrini et al. 2014; Panesar et al. 2016; Zheng et al. 2017; Yang & Chen 2019). Zhang et al. (2001) discovered that when major solar eruption event (a giant filament eruption, a great flare, or an extended Earth-directed coronal mass ejection) happened, the only obvious magnetic change over the course of the event is magnetic flux cancellation at many sites in the vicinity of the filament. Li et al. (2015) found that the location of emerging flux within the filament channel is probably crucial to filament eruption. They suggested that if the flux emergence appeared

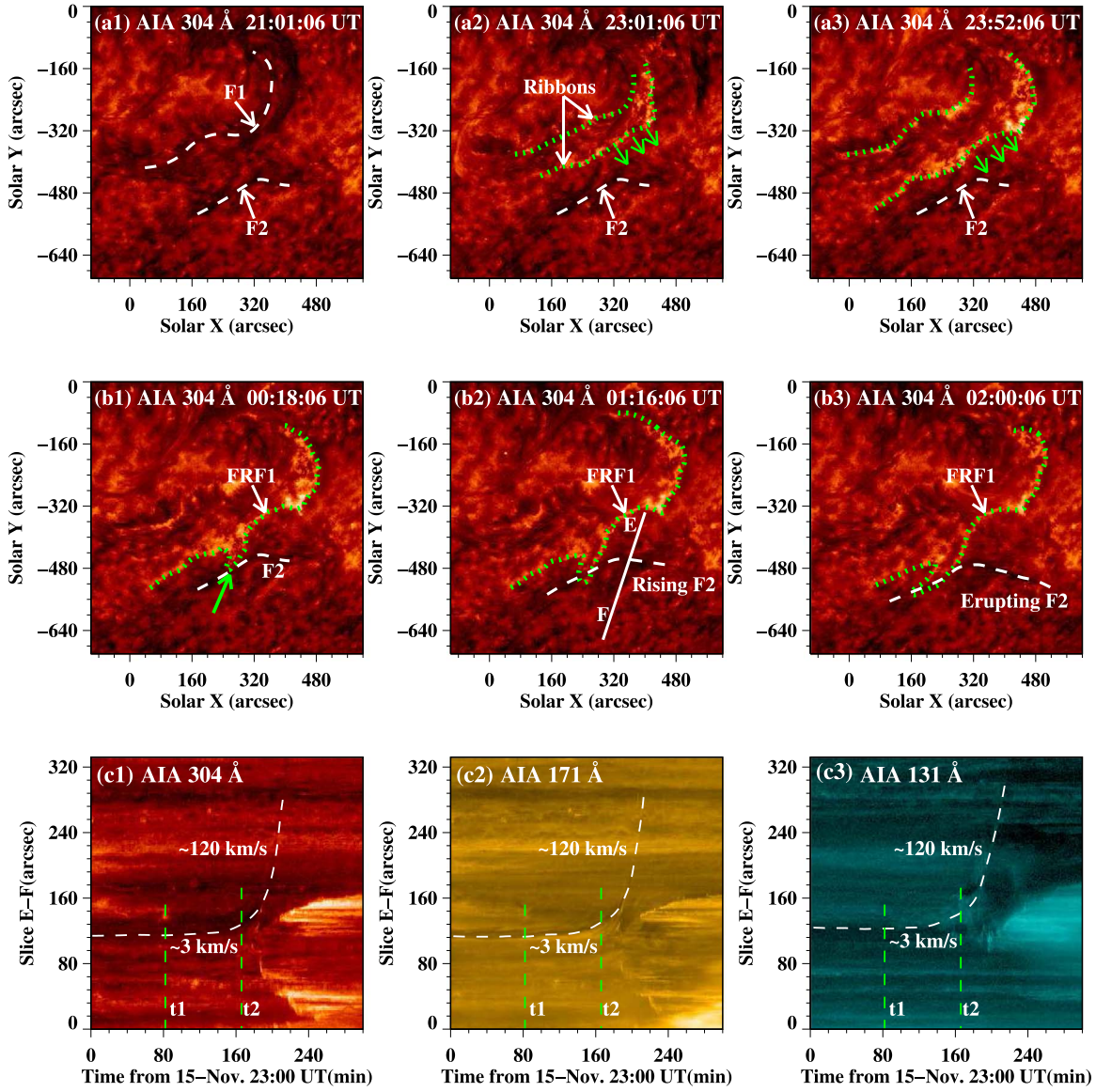

Figure 4. Temporal evolution of FRF1 spreading, FRF1 and F2 interacting, and F2 erupting. Panels (a1)–(a3): time sequences of 304 Å images showing the expansion of the flare ribbons formed by F1 eruption. In panel (a1), the approximate locations of F1 and F2 before their eruptions are outlined by white dashed curves. The green dotted curves in panels (a2)–(a3) display the separating flare ribbons related to F1's eruption. The green arrows in panels (a2)–(a3) indicate the spreading direction of the southwestern ribbon. Panels (b1)–(b3): time sequences of 304 Å images displaying the lifting and eruption of F2 by the intrusion of the southwestern flare ribbon (FRF1) related to eruptive F1. The green arrow in panel (b1) denotes the location where FRF1 reached and invaded F2. The line "E-F" in panel (b2) marks the position of time-slice plots in panels (c1)–(c3). Panels (c1)–(c3): time slices of AIA 304, 171, and 131 Å images revealing the temporal evolution of F2. The animation shows the spreading of FRF1, the interaction between FRF1 and F2, and the eruption of F2 from 00:00 to 02:00 UT on 2015 November 16 in the 304, 171, and 131 Å images. The real time duration of the video is 12 s.

(An animation of this figure is available.)

near a filament's barbs, flux cancellation was prone to occur, which probably caused the filament eruption. In the present work, prior to the eruption of F1, obvious magnetic flux cancellation and emission brightening could be observed in the F1 channel (Figure 2). When the emission reached the peak, F1 began to erupt (see the dotted vertical white line in Figure 3(b1)). Thus, we suggest that the flux cancellation happening in F1 channel results in F1 eruption.

As mentioned above, a filament probably erupts due to the magnetic flux emergence and cancellation. If there is another stable filament located just beside this erupting filament coincidentally, the interaction between these two filaments usually is inevitable and the direct collision would result in the eruption of the second filament (Bone et al. 2009; Zheng et al. 2017). However, differing from the filament-filament interactions, the sympathetic filament eruptions occur without direct touching between the bodies of filaments or the material of filaments (Bumba & Klvana 1993; Wang et al. 2001; Lugaz et al. 2017). The exact nature of sympathetic eruptions is still a controversial issue. Observational investigations (Jiang et al. 2011; Shen et al. 2012; Joshi et al. 2016; Wang et al. 2018) and numerical simulations (Ding et al. 2006; Török et al. 2011; Lynch & Edmondson 2013) suggest that magnetic reconnections of large-scale magnetic fields, which are induced indirectly or directly by distant or nearby eruptions, may be the crucial physical links between sympathetic eruptions, for

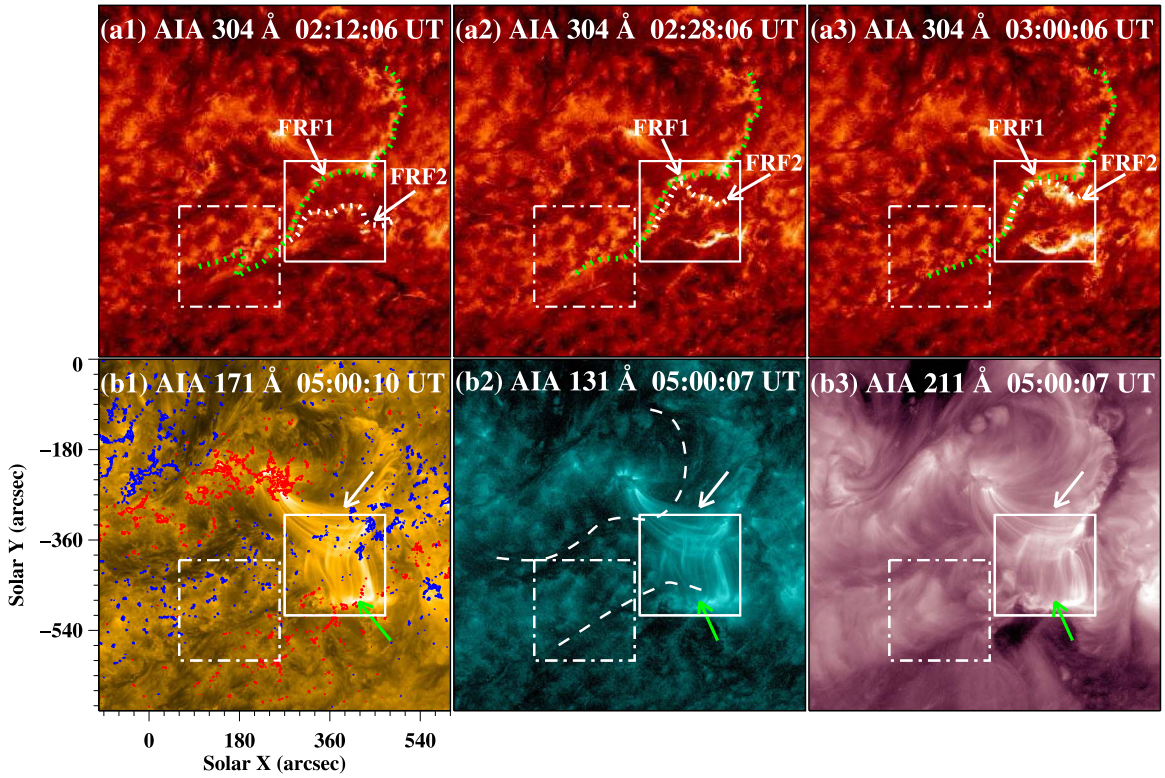

Figure 5. Temporal evolution of FRF2 and post-flare loops after F2's eruption. Panels (a1)–(a3): time sequences of AIA 304 Å images showing the process of the northern ribbon (FRF2; white dotted curves) related to F2's eruption approaching the southwestern ribbon (FRF1; green dotted curves) formed by F1's eruption. Panels (b1)–(b3): AIA 171, 131, and 211 Å images displaying the post-flare loops caused by the eruptions of F1 and F2. The red and blue curves in panel (b1) are contours of corresponding HMI LOS magnetic fields with positive and negative polarity, respectively. The contour levels are ±50 G. The white and green arrows in panels (b1)–(b3) indicate the post-flare loops formed after the eruptions of F1 and F2, respectively. The dashed curves in panel (b2) denote the approximate locations of F1 and F2 before their eruptions. The white and dashed–dotted squares in all panels outline two different regions northwest and southeast of F2, respectively. The animation shows the formation and spread of FRF2, and the post-flare loops caused by the eruptions of F1 and F2 from 02:00 to 04:59 UT on 2015 November 16 in the 304, 171, and 131 Å images. The real time duration of the video is 18 s.

(An animation of this figure is available.)

the reconnections could weaken and partially remove the overlying magnetic fields on the other filaments, resulting in their destabilization and eruptions.

In this work, F2 began to erupt about 100 minutes after FRF1 intruded the southeast region of F2 (see Figures 4(b1)–(b3)). And then we observed two different manifestations in the northwest and southeast regions of F2. There were clear flare ribbons formed by the eruptive F2 in the northwest area of F2, which spread north and south, respectively, and the northern one extended to the edge of FRF1 (see Figure 5(a3)). Meanwhile, clear post-flare loops were also observed in the northwest region of F2. But neither clear flare ribbons nor obvious post-flare loops could be observed in the southeast area of F2 (see Figure 5, and the online animation of Figure 5). These observational results imply that the distribution of the overlying magnetic fields of F2 is not uniform, i.e., the overlying magnetic fields of F2 are stronger in its northwest area, but weaker in its southeast region. The NLFFF reconstructions support the observations and our speculation that the overlying magnetic fields of F2 are not uniform (see Figure 6). As shown in Figure 4 and its corresponding movie, the northwestern part of FRF1 ceased its apparent motion to the southwest at about 23:50 UT on November 15; meanwhile the southwestern part of FRF1 kept moving southwest, approaching the site of F2. We suggest that it is possible that the stronger overlying magnetic fields of F2 in the northwest area partially blocked FRF1 from expanding further southwest. In contrast, the weaker overlying magnetic fields in the southeast region of F2 made F2 more sensitive to external disturbances happening in that region. As a result, when the southeast part of FRF1 continuously invaded the southeast site of F2, F2 was disturbed to slowly rise and eventually erupt. Note that AIA observations of the full eruption of F2 show that no active eruption is clearly observed in the southeast part of F2 at the initial phase. The possible reasons for this, in our opinion, are as follows: first, the speed at which F2 started to rise is too low to distinguish clearly. Second, as shown in the Hα observations, the plasma density of F2 in the southeast region is much less than that in the northwest region (see Figure 1(a)). So it is reasonable that the eruption of F2 appeared more obviously in the northwest region even though it started in the southeast region. Finally, the projection effect may also make a difference here, causing the observations to differ from reality.

Because no direct touch between F1 and F2 was observed, we conjecture that the interaction occurring between F1 and F2 is sympathetic. And the causal link of the sympathetic interaction is that FRF1 invades the southeastern region of F2, where the overflying magnetic fields of F2 are very weak. Based on the multi-wavelength observations, we present a schematic diagram in Figure 7 to illustrate this sympathetic eruption event. The difference of field line density in Figure 7 is used to indicate the non-uniform distribution of the overlying

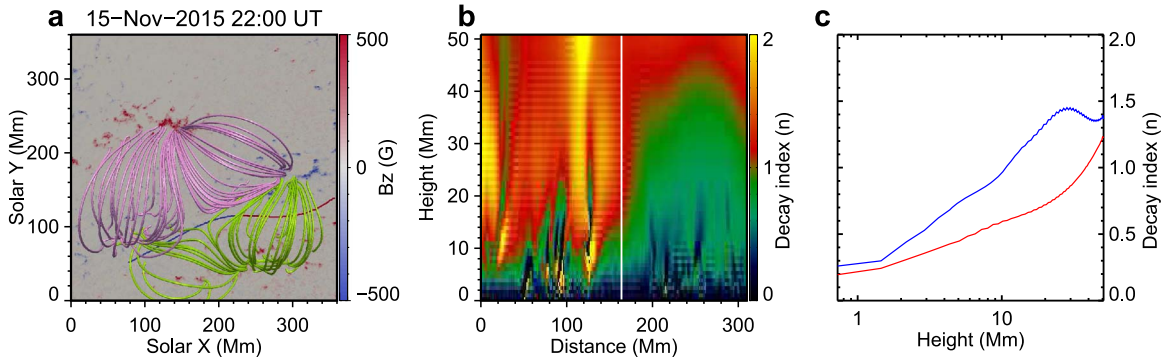

Figure 6. Results of the NLFFF reconstruction of the overlying magnetic fields of F1 and F2. Panel (a): top view of the magnetic fields above F1 and F2. Pink and green curves represent the overlying magnetic field lines of F1 and F2, respectively. The blue–red curve marks the magnetic neutral line related to F2, and the blue and red segments correspond to the southeast and northwest regions of F2, respectively. Panel (b): the horizontal magnetic field decay index distribution in the vertical plane above the blue–red curve labeled in panel (a). The left (right) side of the white vertical line corresponds to the southeast (northwest) region of F2. Panel (c): the decay index of overlying horizontal magnetic fields of F2 as a function of height in two different regions. The blue curve indicates the southeast region, and the red one indicates the northwest region.

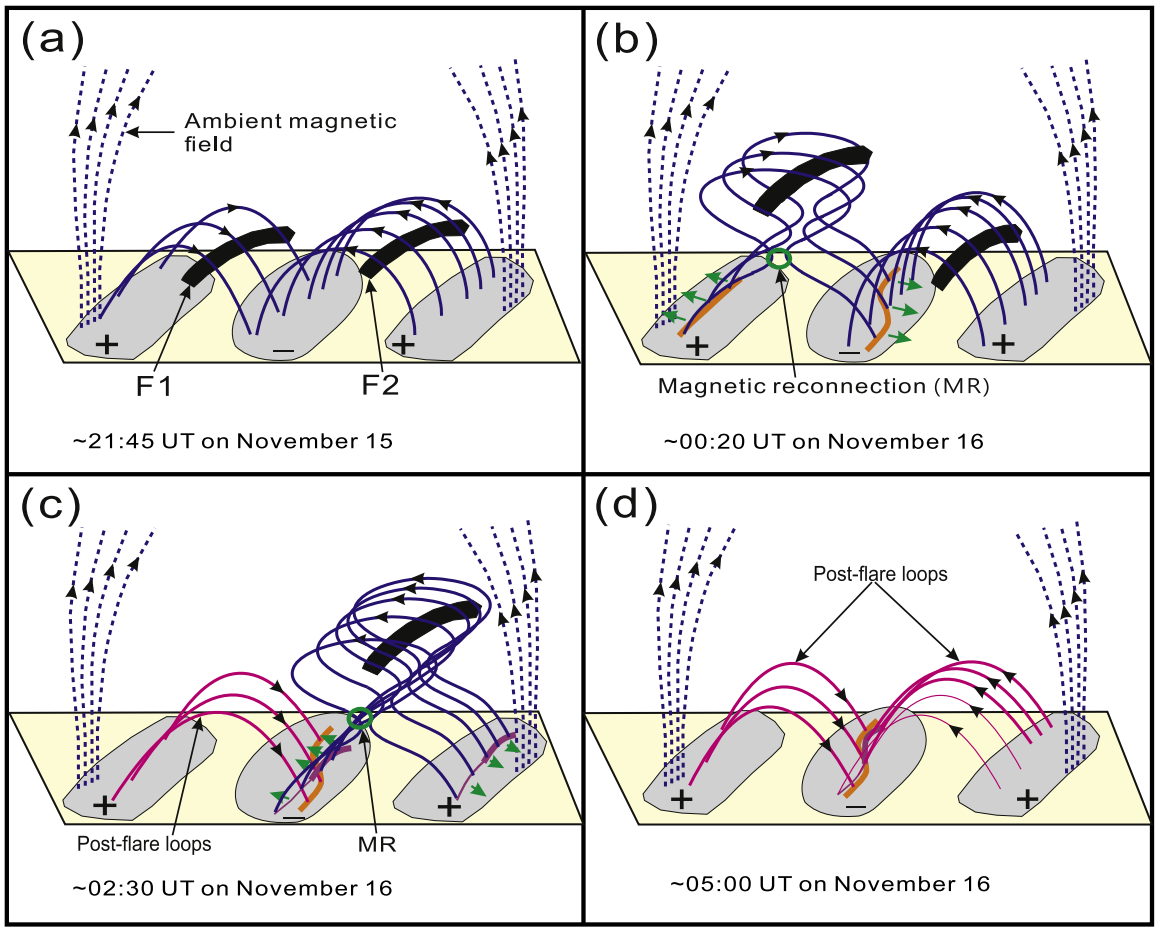

Figure 7. Schematic diagram illustrating the sympathetic eruption event. Panel (a): the initial magnetic configuration of filaments F1 and F2. Panel (b): the eruption of F1 and spreading of flare ribbons. The green arrows in panel (b) indicate the spreading direction of the flare ribbons formed by F1's eruption. Panels (c): the eruption of F2 and spreading of flare ribbons. The green arrows in panel (c) show the spreading direction of the flare ribbons related to F2's eruption. Panel (d): post-flare loops and approaching flare ribbons after the eruptions of F1 and F2. In all panels, the blue dashed curves represent the ambient magnetic field lines. The orange curves in panels (b)–(d) show the flare ribbons formed by F1's eruption. The purple curves in panels (c) and (d) indicate the flare ribbons related to F2's eruption. The green circles in panels (b) and (c) display the sites of magnetic reconnection.

magnetic fields of F2. Panel (a) represents the initial magnetic topology of the two filaments and the overlying ambient coronal fields. Flux cancellation happening around the barbs of F1 disturbs F1 (see Figure 2) and results in its final eruption (see Figure 3). Then two flare ribbons are formed after the eruption of F1, one of which keeps spreading toward F2, intruding and disturbing the magnetic system of F2 in its southeast area (panel (b)). As the overlying magnetic fields of F2 are very weak in the disturbed location, the successive disturbance destabilizes F2, and F2 eventually erupts (panel (c),

also see Figure 4). After the eruption of F2, the clear flare ribbons (shown by the thick purple curves) and post-flare loops (shown by the thick red curves in panel (d)) only appear in F2's northwest region, where the overlying magnetic fields are strong (panels (c) and (d), also see solid squares in Figure 5). And the thin purple and red curves in panels (c) and (d), respectively, are employed to indicate the ambiguous flare ribbons and post-flare loops in F2's southeast area, where the overlying magnetic fields are very weak (also see the dashed–dotted squares in Figure 5).

In the existing reports on sympathetic filament eruptions, the directly observable criterion is mostly the correlation of the eruptive time between two filaments. Joshi et al. (2016) interpreted two successive eruptions as sympathetic eruptions, which occurred in different active regions and were associated by a chain of magnetic reconnections. A fast rise of the second filament beginning soon after the first filament eruption was suggested to be a sympathetic eruption by Li et al. (2017). In the present work, in addition to the temporal correlation, an identifiable causal link between two sympathetic eruptive filaments was observed. To our knowledge, similar observations have never been reported before.

The authors are grateful to the anonymous referee for valuable suggestions. SDO is a mission of NASA's Living With a Star (LWS) Program. AIA and HMI data are courtesy of the NASA/SDO science teams. This work is supported by the National Natural Science Foundations of China (U1531113, 11903050, 11533008, 11790304, 11773039, 11673035, 11673034, 11873059, and 11790300), the open topic of the Key Laboratory of Solar Activities of the Chinese Academy of Sciences (KLSA201902), the National Key R&D Program of China (2019YFA0405000), the B-type Strategic Priority Program of the Chinese Academy of Sciences, Grant No. XDB41000000, the NAOC Nebula Talents Program, and Key Programs of the Chinese Academy of Sciences (QYZDJ-SSW-SLH050).

ORCID iDs

Zhiping Song https://orcid.org/0000-0003-3487-2360
Yijun Hou https://orcid.org/0000-0002-9534-1638

References

Aulanier, G., Török, T., Démoulin, P., & DeLuca, E. E. 2010, ApJ, 708, 314
Biesecker, D. A., & Thompson, B. J. 2000, JASTP, 62, 1449
Bone, L. A., van Driel-Gesztelyi, L., Culhane, J. L., et al. 2009, SoPh, 259, 31
Borrero, J. M., Tomczyk, S., Kubo, M., et al. 2011, SoPh, 273, 267
Bumba, V., & Klvana, M. 1993, Ap&SS, 199, 45
Chen, Y., Du, G., Zhao, D., et al. 2016, ApJL, 820, L37
Cheng, X., & Ding, M. D. 2016, ApJS, 225, 16
Dacie, S., Török, T., Démoulin, P., et al. 2018, ApJ, 862, 117
Dechev, M., Koleva, K., & Duchlev, P. 2018, NewA, 59, 45
Ding, J. Y., Hu, Y. Q., & Wang, J. X. 2006, SoPh, 235, 223
Duchlev, P., Dechev, M., & Koleva, K. 2019, BlgAJ, 30, 99
Filippov, B. 2018, MNRAS, 475, 1646
Gary, G. A., & Hagyard, M. J. 1990, SoPh, 126, 21
Harvey, J. W., Bolding, J., Clark, R., et al. 2011, American Astronomical Society, SPD meeting, 42, 17.45
Hassanin, A., & Kliem, B. 2016, ApJ, 832, 106
Hou, Y., Zhang, J., Li, T., et al. 2016, ApJL, 829, L29
Hou, Y. J., Zhang, J., Li, T., et al. 2018, A&A, 619, A100
Jiang, Y., Yang, J., Hong, J., Bi, Y., & Zheng, R. 2011, ApJ, 738, 179
Jiang, Y., Yang, J., Wang, H., et al. 2014, ApJ, 793, 14
Joshi, N. C., Schmieder, B., Magara, T., Guo, Y., & Aulanier, G. 2016, ApJ, 820, 126
Kliem, B., Su, Y. N., van Ballegooijen, A. A., & DeLuca, E. E. 2013, ApJ, 779, 129
Kliem, B., & Török, T. 2006, PhRvL, 96, 255002
Kliem, B., Török, T., Titov, V. S., et al. 2014, ApJ, 792, 107
Kopp, R. A., & Pneuman, G. W. 1976, SoPh, 50, 85
Leka, K. D., Barnes, G., Crouch, A. D., et al. 2009, SoPh, 260, 83
Lemen, J. R., Title, A. M., Akin, D. J., et al. 2012, SoPh, 275, 17
Li, S., Su, Y., Zhou, T., et al. 2017, ApJ, 844, 70
Li, T., Zhang, J., & Ji, H. 2015, SoPh, 290, 1687
Lugaz, N., Temmer, M., Wang, Y., & Farrugia, C. J. 2017, SoPh, 292, 64
Lynch, B. J., & Edmondson, J. K. 2013, ApJ, 764, 87
Mackay, D. H., Karpen, J. T., Ballester, J. L., Schmieder, B., & Aulanier, G. 2010, SSRv, 151, 333
Mandrini, C. H., Schmieder, B., Démoulin, P., Guo, Y., & Cristiani, G. D. 2014, SoPh, 289, 2041
Martin, S. F. 1998, SoPh, 182, 107
Metcalf, T. R. 1994, SoPh, 155, 235
Miklenic, C. H., Veronig, A. M., Vršnak, B., et al. 2007, A&A, 461, 697
Moore, R. L., Sterling, A. C., Hudson, H. S., & Lemen, J. R. 2001, ApJ, 552, 833
Panesar, N. K., Sterling, A. C., Moore, R. L., & Chakrapani, P. 2016, ApJL, 832, L7
Pesnell, W. D., Thompson, B. J., & Chamberlin, P. C. 2012, SoPh, 275, 3
Porfir'eva, G. A., & Yakunina, G. V. 2013, Ge&Ae, 53, 977
Riley, P., Lionello, R., Linker, J. A., et al. 2011, SoPh, 274, 361
Schmieder, B., Démoulin, P., & Aulanier, G. 2013, AdSpR, 51, 1967
Schou, J., Scherrer, P. H., Bush, R. I., et al. 2012, SoPh, 275, 229
Schrijver, C. J., & Title, A. M. 2011, JGRA, 116, A04108
Shen, Y., Liu, Y., & Su, J. 2012, ApJ, 750, 12
Shibata, K., & Magara, T. 2011, LRSP, 8, 6
Sinha, S., Srivastava, N., & Nandy, D. 2019, ApJ, 880, 84
Sterling, A. C., Moore, R. L., & Freeland, S. L. 2011, ApJL, 731, L3
Su, J., Liu, Y., Kurokawa, H., et al. 2007, SoPh, 242, 53
Sun, J. Q., Cheng, X., Ding, M. D., et al. 2015, NatCo, 6, 7598
Török, T., Panasenco, O., Titov, V. S., et al. 2011, ApJL, 739, L63
Wang, D., Liu, R., Wang, Y., et al. 2018, ApJ, 869, 177
Wang, H., Chae, J., Yurchyshyn, V., et al. 2001, ApJ, 559, 1171
Wang, R., Liu, Y. D., Zimovets, I., et al. 2016, ApJL, 827, L12
Wheatland, M. S., Sturrock, P. A., & Roumeliotis, G. 2000, ApJ, 540, 1150
Wiegelmann, T. 2004, SoPh, 219, 87
Woods, M. M., Inoue, S., Harra, L. K., et al. 2018, ApJ, 860, 163
Yang, B., & Chen, H. 2019, ApJ, 874, 96
Yang, J., Jiang, Y., Zheng, R., et al. 2012, ApJ, 745, 9
Yang, L., Yan, X., Li, T., Xue, Z., & Xiang, Y. 2017, ApJ, 838, 131
Yang, S., & Zhang, J. 2018, ApJL, 860, L25
Zaitsev, V. V., & Stepanov, A. V. 2018, JASTP, 179, 149
Zhang, J., Wang, J., & Nitta, N. 2001, ChJAA, 1, 85
Zheng, R., Zhang, Q., Chen, Y., et al. 2017, ApJ, 836, 160
Zirker, J. B., Martin, S. F., Harvey, K., & Gaizauskas, V. 1997, SoPh, 175, 27